



PRODUCTION OF OXIDE DISPERSION STRENGTHENED INCONEL 718 ALLOYS USING CONVENTIONAL POWDER METALLURGY AND ADDITIVE MANUFACTURING METHODS

*Eda AYDOĞAN 

Middle East Technical University, Metallurgical and Materials Engineering Department, Ankara,
TÜRKİYE
aydogane@metu.edu.tr

Highlights

- ODS IN718 alloys were produced by powder metallurgy and SLM additive manufacturing
- PM samples have nanograins with high-density homogenously distributed nano-oxides
- SLM samples have cellular structure and high-density grouped nano-oxides
- Nano-oxides are determined to be mostly $Y_2Ti_2O_7$, Y_2TiO_5 or $YTiO_3$ and Y-Al-O
- There are bi-phase particles in SLM-produced alloys due to rapid cooling



PRODUCTION OF OXIDE DISPERSION STRENGTHENED INCONEL 718 ALLOYS USING CONVENTIONAL POWDER METALLURGY AND ADDITIVE MANUFACTURING METHODS

*Eda AYDOĞAN

Middle East Technical University, Metallurgical and Materials Engineering Department, Ankara, TÜRKİYE
aydogane@metu.edu.tr

(Received: 22.02.2023; Accepted in Revised Form: 11.05.2023)

ABSTRACT: Oxide dispersion strengthened (ODS) Ni-based alloys having a high density of nano-oxides (NOs) (<10 nm) are considered to be good candidates for extreme environments, such as high temperature, radiation, and corrosion. In this study, ODS IN718 alloys have been produced using conventional powder metallurgy (PM) and novel selective laser melting (SLM) additive manufacturing. The effect of processing routes on the microstructure, in particular on the nano-oxide formation and structure has been investigated. It has been found that the powder metallurgy method that consists of compressing followed by sintering at 1250 and 1500 °C results in a nano-granular structure with homogenously distributed fine nano-oxides having a high number density. Similarly, SLM results in a high number density of fine nano-oxides; however, the particles exist in groups with the grains/cells. The nano-oxides are determined to be $Y_2Ti_2O_7$, Y_2TiO_5 or $YTiO_3$ and Y-Al-O. The deviation in the lattice parameters of $Y_2Ti_2O_7$ infers the existence of some Al in the structure. This study sheds light on producing ODS IN718 alloys with high-density nano-oxides using powder metallurgy and additive manufacturing methods.

Keywords: Additive Manufacturing, Inconel 718, Nano-Particle, Oxide Dispersion Strengthened Alloy, Powder Metallurgy, Transmission Electron Microscopy

1. INTRODUCTION

Ni-based superalloys have been widely used for extreme applications such as gas turbines, turbo motors and nuclear reactors due to their high strength and creep resistance at high temperatures, thermal stability and high corrosion resistance [1, 2]. Even though they have exceptional properties up to ~700 °C, the properties degrade suddenly above this temperature as a result of coarsening and dissolution of strengthening phases, namely γ' and γ'' . On the other hand, oxide dispersion strengthened (ODS) alloys have shown exceptional thermal stability above 1000 °C and almost zero radiation-induced swelling due to the existence of high-density nano-oxides having sizes less than 5 nm [3, 4]. These nano-oxides are reported to pin the dislocations and grain boundaries impeding grain growth and recrystallization, thus improving the high temperature stability and creep resistance. Moreover, the high number density of fine nano-particles provides a large interfacial area acting as the sinks for point defects [5-7].

The nano-oxides are mostly in $Y_2Ti_2O_7$ and Y_2TiO_5 form in Al-free ferritic systems [4, 8]. On the other hand, Y-Al-O particles with YAP ($YAlO_3$, perovskite), YAG ($Y_3Al_5O_{12}$, garnet), YAM ($Y_4Al_2O_9$, monoclinic), YAP ($YAlO_3$, pseudo-perovskite), YAH ($YAlO_3$, hexagonal), and YAT ($Y_3Al_5O_{12}$, tetragonal) structures have been reported in the ferritic alloys such as MA956 having up to ~6 wt.% Al [9]. Moreover, Park et al. have studied spark plasma sintered ODS Ni-based alloys and found the formation of $Y_2Ti_2O_7$ and complex Y-Al oxides such as $Y_4Al_2O_9$ and $Y_3Al_5O_{12}$ [10].

The composition and production method of the ODS alloys determine the final properties of the alloys. The Oxygen content of the material has a profound effect on the size and number density of nano-oxides [11]. Moreover, the nano-oxide size has been reported to be coarser in the existence of Al in the system [10]. ODS alloys are conventionally produced by powder metallurgy methods such as ball milling followed by hot pressing, hot rolling, hydrostatic extrusion, spark plasma sintering etc. [10, 12, 13] which result in fine microstructures with superior high temperature mechanical properties. For instance, Hoelzer

et al. and Miller et al. have produced 14YWT ferritic alloys using consolidation, hot extrusion and annealing steps, and these alloys have microstructural stability up to ~ 1300 °C and tensile and creep strength up to 800 °C [12, 14]. Furthermore, Nickel-based ODS alloys have been reported to show improved tensile strength as a result of the refinement in grain size due to the existence of Al [15]. However, conventional powder metallurgy methods consist of many steps, thus they are both time intensive and expensive.

Additive manufacturing (AM) methods such as selective laser melting (SLM), laser directed energy deposition (LDED), and electron beam melting (EBM) have been developed to produce complex-shaped alloys with high densification in a near net-shaped state [16, 17]. However, due to the high thermal gradients during the AM processes, columnar-shaped grains are formed along the building direction of the materials which causes anisotropic properties [18]. There is an immense literature to solve this problem. For instance, Oliveira et al. [19] studied the process parameters to control the microstructure. Ni et al. [20] Popovich et al. [21] and Tillmann et al. [22] investigated post-processing methods such as heat treatments and hot isostatic pressing to modify the as-built microstructure after additive manufacturing. On the other hand, nano-particle reinforcement has been reported to hinder columnar structure formation, reducing the texture in the AM samples [23, 24]. Besides controlling the microstructure, nano-particle dispersion improves high temperature strength and creep resistance of the materials [25, 26]. Studies on the development of nano-particle reinforced metal alloys using additive manufacturing have been increasing. For example, 17-4 PH steels with high number density TiN particles have been produced using SLM [27]. Moreover, ferritic ODS Fe14Cr as well as Nickel-based ODS IN738LC, NiCrFeY and Hastelloy X have been produced by SLM [28-31]. Recently, we have produced ODS IN718 alloys having different compositions using SLM and reported their behavior under heavy ion irradiation at 200 and 450 °C [32, 33]. However, the particle size of the AM produced ODS alloys is coarser and the number density of the particles is smaller compared to the conventional PM produced alloys, with the nano-oxide density in the order of $\sim 10^{23}$ m⁻³.

In this study, ODS-IN718 alloys which were designed in our previous studies have been produced using both conventional powder metallurgy method of compression followed by sintering and novel SLM additive manufacturing methods. Detailed microstructural analyses have been conducted to determine the type of nano-particles as well as their size and number density in PM and SLM produced alloys. It has been found that both PM and SLM methods result in a high number density of Y₂Ti₂O₇, Y₂TiO₅ or YTiO₃ and Y-Al-O, except for the difference in their distribution. This is the first study comparing the microstructure, especially the nano-particles forming as a result of PM and AM production methods to the best of the author's knowledge.

2. MATERIAL AND METHODS

In this study, spherical IN718 powders having 20-55 μ m size were used for conventional powder metallurgy and additive manufacturing methods. The powders were provided by EOS GmbH. Moreover, Y₂O₃ nano-powders having the size of 18-38 nm were provided by Nanografi Nanotechnology Co. The composition of the IN718 powders is measured as 53Ni-17.7Fe-19.4Cr-5.1Nb-3.1Mo-0.94Ti-0.46Al-0.1Co-0.1Mn (in wt.%) [33].

First of all, IN718 powders were mixed with 0.3 wt% of Y₂O₃ nano-powders using a Fritsch Pulverisette P6 classic line ball mill without balls operating under Ar atmosphere at 300 rpm for 10 mins. The powders were compressed up to 200 psi in 10 mm diameter cylinders using a uniaxial press followed by sintering at 1000, 1250 and 1500 °C for 10 h. These samples are nominated as PM1000, PM1250 and PM1500. The pre-mixed powders were deposited by SLM layer by layer with a laser power of 220 W and a scan speed of 960 mm/sec using an EOS M 290 machine [33]. Table 1 summarizes the SLM production parameters. After the deposition, the AM parts were removed from the substrate using electro-discharge machining (EDM).

Table 1. SLM production parameters

Parameter	Value
Power (W)	220
Scan speed (mm/sec)	960
Laser spot size (μm)	100
Layer thickness (μm)	40
Hatch spacing (μm)	110
Rotation degree ($^{\circ}$)	67

The density of the samples was measured by Archimedes method in ethanol. The microstructural investigations have been carried out using optical microscopy (OM), scanning electron microscopy (SEM) and transmission electron microscopy (TEM). For the metallographic investigations, the samples were coarse grinded to determine the efficiency of the sintering parameters. Detailed OM and SEM analyses were conducted on the samples grinded and polished down to $0.04 \mu\text{m}$ colloidal silica followed by etching with 2 ml HNO_3 – 4 ml HCl – 4 ml HF solution. OM analyses were carried out using a Huvitz HDS-5800 digital microscope while a FEI Nova Nano SEM 430 was used for SEM investigations. The composition of second phase particles was determined using energy dispersive X-ray spectroscopy (EDX) with EDAX SSDD Apollo10 EDX system under SEM. Data collection times during point analyses for each precipitate were at least 60 s to be able to get high peak-to-background ratios. After the polishing step, TEM samples were punched into 3 mm disks which were electropolished using 95% methanol – 5% perchloric acid solution at $-40 \text{ }^{\circ}\text{C}$ with a 15-18 V. TEM analyses were conducted using a JEOL JEM-ARM200CFEG UHR-TEM.

Microhardness tests were performed using a Shimadzu HMV-2 E microhardness tester with 1 kg load and 10 s holding time. At least 10 indents were taken from different locations on the surface of the samples.

3. RESULTS AND DISCUSSION

IN718 powders and the oxide former (Y_2O_3) were mixed before production. In the case of powder bed fusion processes, the shape of the powder is critical for the flowability which determines the quality of the production. Thus, the sphericity of the powders should be kept during mixing which was also reported by Karakilinc et al. [34]. Figure 1 shows the morphology of the powders after mixing in a ball mill for 10 mins as described in the previous section. The Y_2O_3 nano-powders pointed by the red arrows in a zoomed micrograph are attached to the spherical IN718 micro-powders forming satellites.

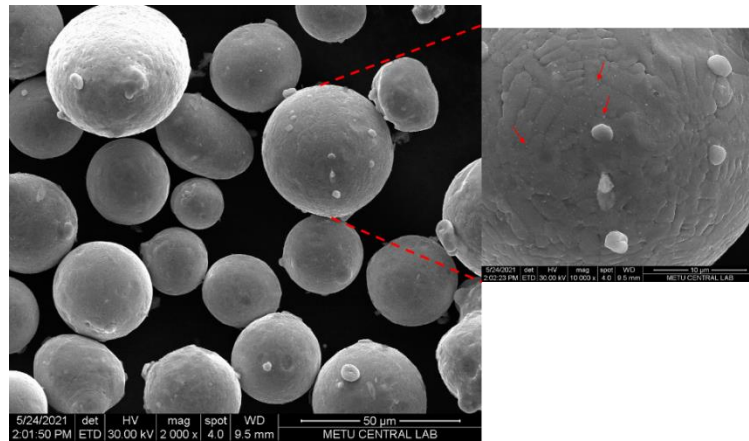


Figure 1. SEM micrographs showing the morphology of the powders after mixing in a ball mill for 10 mins.

Figure 2(a-c) shows the microstructure of PM samples after sintering at 1000, 1250 and 1500 °C for 10h. Clearly, 1000 °C is not enough for obtaining a dense material, while dense materials (>99.6%) can be produced after sintering at 1250 and 1500 °C for 10 h. Moreover, the hardness of the samples presented in Figure 2d indicates that porosity in the case of PM1000 sample deteriorates the mechanical properties. Besides, PM1500 sample exhibits the highest hardness which is ~30HV higher than the hardness of PM1250. This will be further investigated in the following sections. It should be noted that high-porosity PM1000 samples have not been considered for future studies.

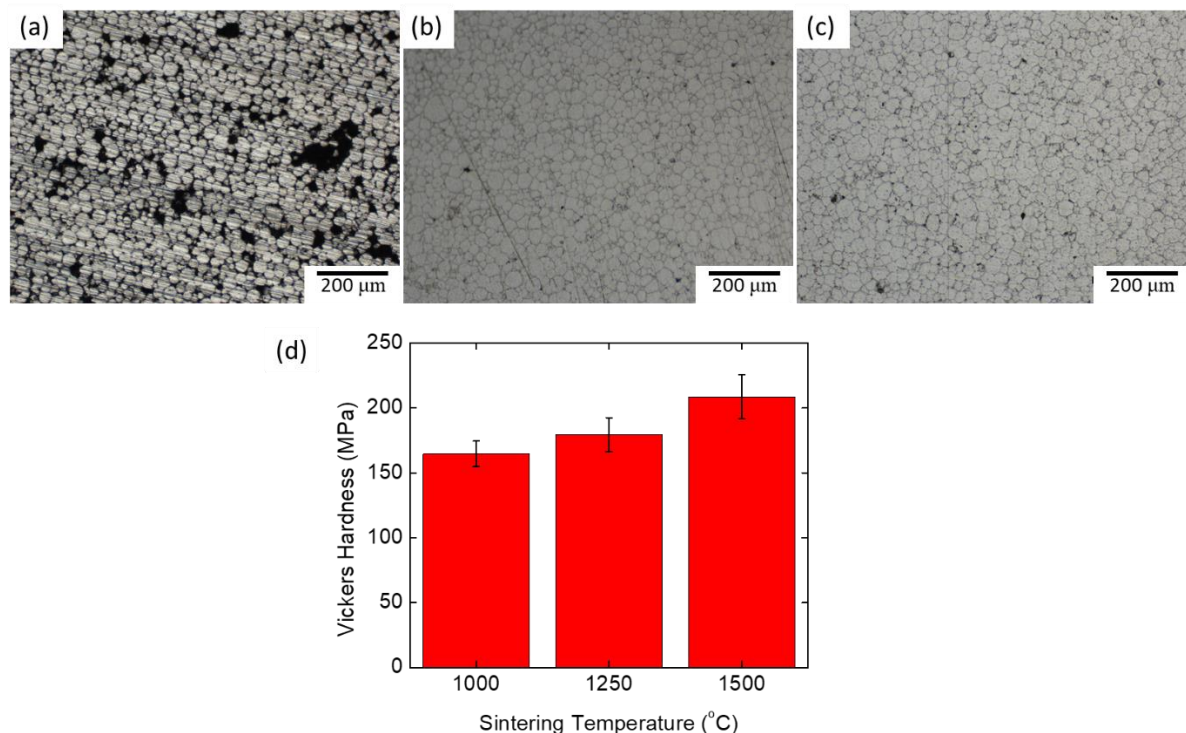


Figure 2. OM images of PM samples sintered at (a) 1000 °C (b) 1250 °C (c) 1500 °C for 10 h; and (d) microhardness plot with respect to the sintering temperature.

Figure 3 shows the SEM (Figure 3(a-c)) and OM micrographs (Figures 3(d-g)) of PM1250, PM1500 and SLM samples. Figure 3 (a-c) shows the SEM micrograph of the PM1250 sample. Even though there are a few empty triple junctions, the space between the powders is well covered. At high magnifications, the existence of nano-particles especially around the grain boundaries, is seen. Similarly, besides a small

amount of porosity, PM1500 sample is dense and there are spherical-shaped particles that are coarser compared to the ones in PM1250 sample (Figures 3d and e). Figures 3f and g show the microstructure of the additively manufactured alloy. The microstructures of PM and SLM produced alloys are quite different. While the PM alloys show the powders sintered each other with spherical shapes, SLM produced sample shows melt pools having a thickness of $\sim 100 \mu\text{m}$ indicating the deposition layers. Besides, there are Laves phase as well as the carbides and coarse oxide particles. During the SLM process, the cooling rate reaches $\sim 10^6 \text{ K/sec}$. Thus, cellular structure is observed, as seen in Figure 3g.

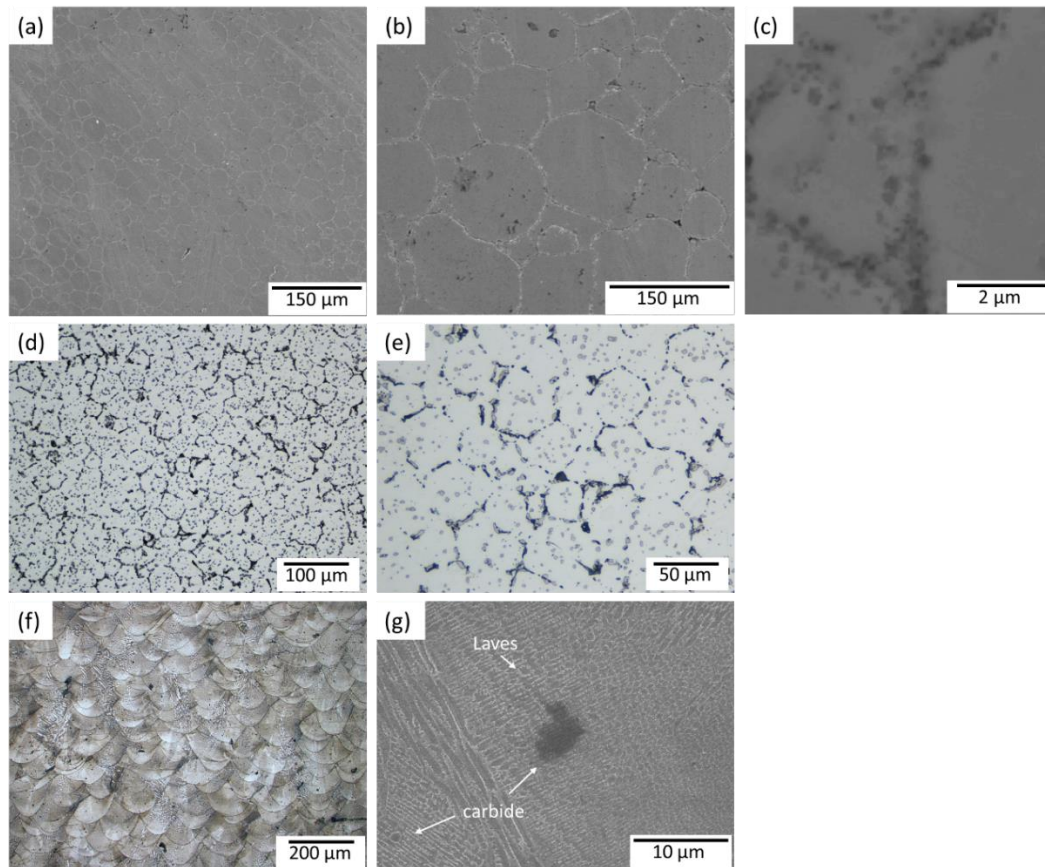


Figure 3. Microstructures of (a-c) PM1250 (d,e) PM1500 and (f,g) SLM alloys.

It has been reported that oxide nano-particles in ODS alloys can stabilize the microstructure by pinning the grain boundaries and dislocations, restricting the recrystallization, grain growth and thus creep. Besides, the interface between the nano-oxides and matrix act as sinks for point defects which results in a reduced amount of radiation damage [5-7]. On the other hand, the size and number density of the particles become critical. The smaller the particle size and the higher the number density of the particles, the better the resistance of the alloy in the extreme conditions. Aydogan et al. have reported that the strength of the ODS ferritic alloys is closely related to the size and number density of the nano-oxides [3]. Furthermore, while the 14YWT alloy having $\sim 7 \text{ nm}$ particle size with a number density in the order of $\sim 10^{21} \text{ m}^{-3}$ shows $\sim 7\%$ of swelling, the same alloy with $\sim 3 \text{ nm}$ particle size and a number density in the order of $\sim 10^{23} \text{ m}^{-3}$ shows almost no swelling [3]. Thus, it is critical to determine the size and number density of the nano-particles after production, and in this study, the nano-particles produced as a result of powder metallurgy and additive manufacturing have been investigated.

Figure 4 presents the TEM micrographs of the PM1250 alloy having a high density of nano-particles mostly with $< 10 \text{ nm}$ size (Figures 4a and b). Figures 4c and d show the high resolution TEM (HRTEM) image of a nano-particle having a diameter $\sim 5 \text{ nm}$ and the corresponding fast fourier transform (FFT) spectrum. Moreover, Figures 4e and f show the HRTEM image of a smaller nano-particle having a

diameter ~ 2 nm and corresponding FTT spectrum. HRTEM images exhibit that while ~ 2 nm size nano-particle has a coherent interface inferred from the continuity of the atomic order, larger size particle has a disruption in coherency. It has been reported that fine dispersoids are most likely to be coherent while the larger particles tend to be incoherent [7, 35, 36]. Moreover, the coherency of the particles has been shown to affect the properties of the materials due to the different interaction mechanisms of these particles with dislocations and grain boundaries. The coherent particles are observed to be efficient in pinning the grain boundaries while the incoherent particles are more capable of restricting the dislocation motion [35, 37-39].

The interplanar distances and angles have been tabulated in Table 2. It has been found that while the larger size particle has the crystal structure of either $Y_2Ti_2O_7$ or $YTiO_3$, the smaller size particle is $Y_2Ti_2O_7$. Similarly, Yu et al. have found that large particles have crystal structures different than pyrochlore $Y_2Ti_2O_7$ and have Y/Ti ratio between 1 to 2 [8]. Furthermore, the size and number density of the nano-oxides in PM1250 sample have been found to be 3.9 ± 0.5 nm and $1.6 \times 10^{22} \text{ m}^{-3}$, respectively.

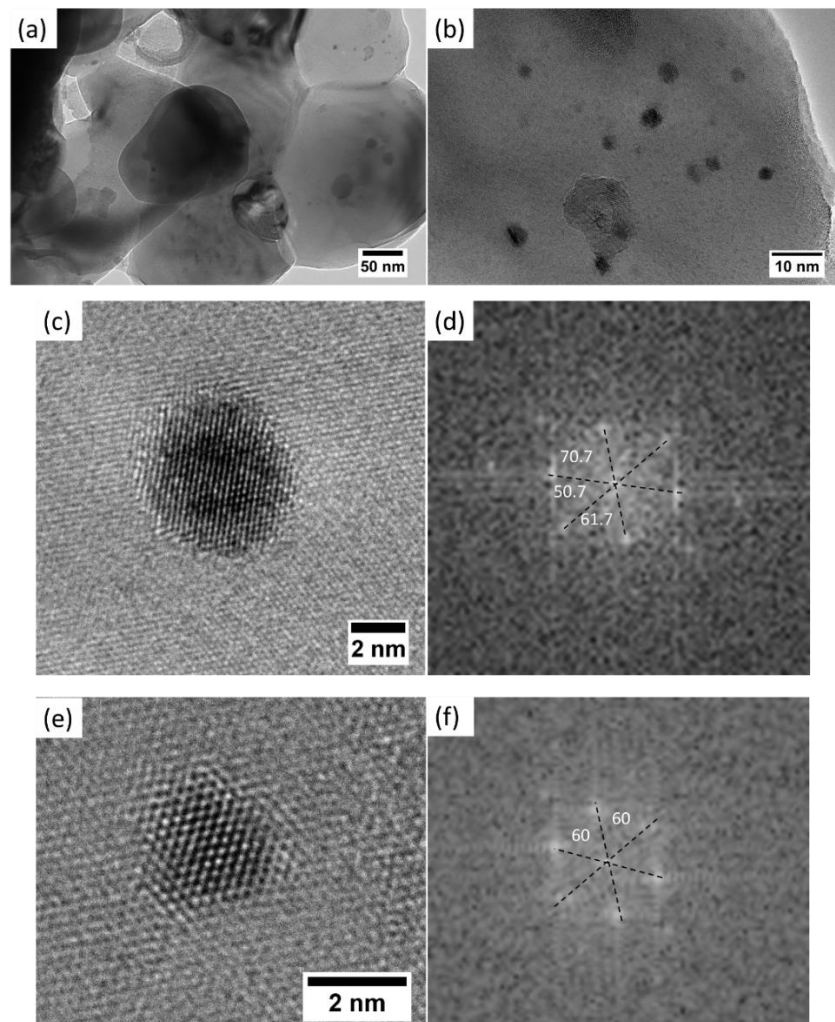


Figure 4. TEM micrographs of PM1250 sample, showing (a) the nano-grains and (b) nano-particles; HRTEM micrographs of (c) a particle with ~ 5 nm size and (d) corresponding FFT spectrum; (e) a particle with ~ 2 nm size and (d) corresponding FFT spectrum.

Table 2. Measured and theoretical interplanar distances and angles for the particles in Figure 4.

		d_1 (Å)	d_2 (Å)	d_3 (Å)	α_{12} (°)	α_{23} (°)	α_{13} (°)
	Measured	2.63	2.06	2.14	61.7	70.7	50.7
Figure 4c	Y ₂ TiO ₅	2.52 (401)	2.09 (313)	2.18 ($\bar{1}\bar{1}\bar{4}$)	62.5	67.6	50.2
	YTiO ₃	2.50 ($\bar{1}20$)	2.09 (202)	2.18 (122)	62.3	67.3	50.4
Figure 4e	Measured	1.92	2.02	2.04	60	60	60
	Y ₂ Ti ₂ O ₇	1.79 (0 $\bar{4}$ 4)	1.79 (404)	1.79 (440)	60	60	60

Sintering at 1250 °C occurs mostly in the solid state while sintering at 1500 °C occurs above the liquidus temperature of IN718, inferring at least a partial melting [33]. To determine if the sintering temperature affects the characteristics of the nano-particles, detailed TEM analyses have been conducted on PM1500 sample. Figures 5a and b exhibit the nano-structure of the alloy. Clearly, the microstructure is composed of nano-grains having a size 100-200 nm and nano-particles having a particle size <30 nm. One of the largest particles has been investigated using HRTEM as seen in Figure 5c. FFT diffraction spectrum indicates that this particle has an FCC crystal structure with a lattice parameter of 14.4 Å, which is identified as Ni₂Y intermetallic. Ni-Y intermetallic phases have been observed in IN625 alloy coated with NiCrAlY using a laser-engineered net shaping (LENS) system. The formation of such intermetallic having different stoichiometry is reported to occur instantaneously directly from the liquid [40-42]. Table 2 shows the measured and theoretical lattice spacing and angles. Figures 5e and f show an HRTEM micrograph of ~7 nm size nano-particle and corresponding FFT diffractogram, respectively. It has been found that the measured interplanar distances and angles in Table 3 are close to the parameters of hexagonal Y-Al-O (PDF# 00-054-0621) whose lattice parameters are, $a = b = 0.368$ nm, $c = 1.052$ nm, and $\gamma = 120^\circ$ [43]. However, the stoichiometry of the observed particle seems to be slightly different which is inferred from the values which are slightly off. It should be noted that Al content of these particles varies considerably and can reach up to ~45 at.% while there is some Titanium (2-5 at.%). Moreover, Figures 5g and h show an HRTEM image and corresponding FFT of another particle having a size of ~7-8 nm. The measured parameters are slightly different than the theoretical values (Table 2). This has been attributed to the existence of Al in the Y-Ti-O particles. Since this particle has a presumably small amount of Al, it may still hold the pyrochlore structure and can be identified as Y₂Ti₂O₇. Clearly, at higher sintering temperatures, Al seems to participate more in the nano-particles, forming Y-Al-O particles as well as Y-Ti(Al)-O particles. It has been reported that when a local melting occurs, Y-Al-O or Y-Ti-O rich in Al particles form [10]. However, this composition in solid-state does not yield the formation of Y-Al-O; rather Y-Ti-O particles rich in Al can exist [33]. This might explain the reason for observing more Y-Ti-O particles in the solid-state sintering case of PM1250.

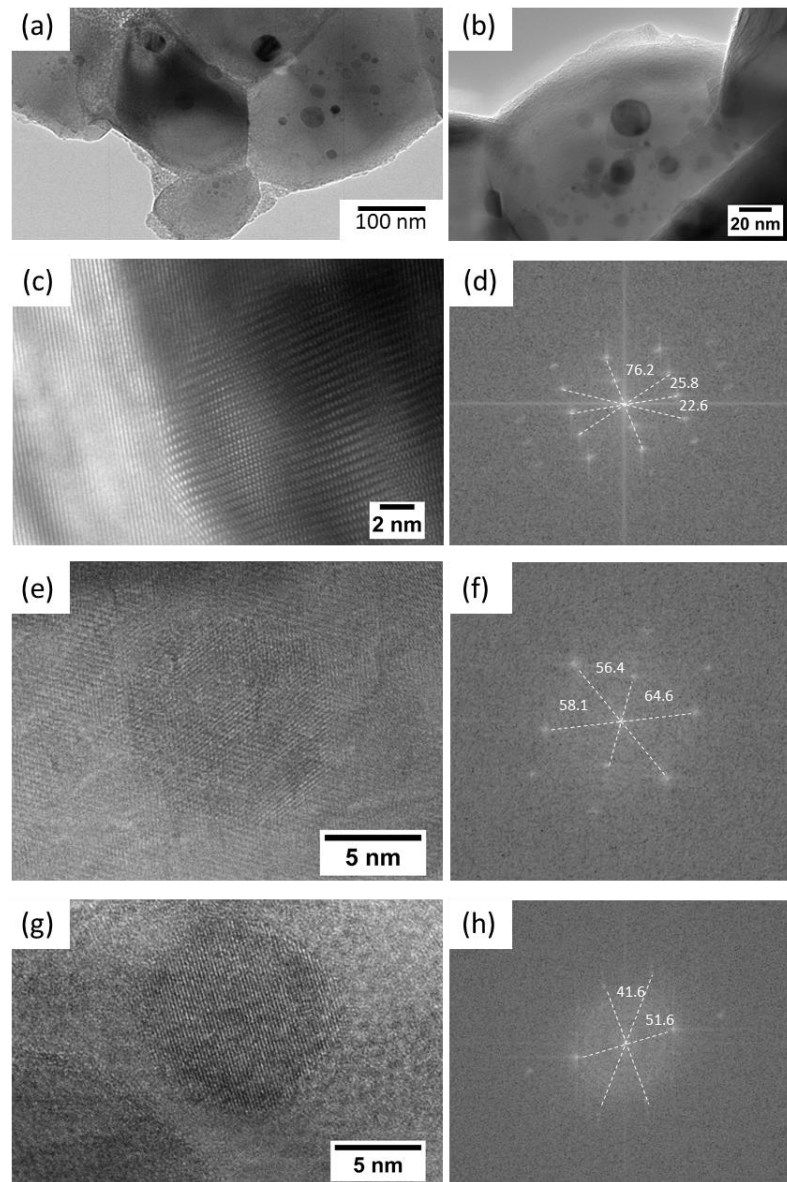


Figure 5. TEM micrographs of PM1500 sample, showing (a) the nano-grains and (b) nano-particles; HRTEM micrographs of (c) a large particle and (d) corresponding FFT spectrum; (e,g) particles with ~7 nm size and (f,h) corresponding FFT spectra.

Table 3. Measured and theoretical interplanar distances and angles for the particles in Figure 5.

		d_1 (Å)	d_2 (Å)	d_3 (Å)	α_{12} (°)	α_{23} (°)	α_{13} (°)
Figure 5c	Measured	2.4	2.4	5.2	25.8	76.2	102
	Ni ₂ Y	2.4 ($\bar{2}4\bar{4}$)	2.4 ($\bar{4}2\bar{4}$)	5.1($\bar{2}\bar{2}0$)	27.3	76.4	103.7
Figure 5e	Measured	2.02	1.97	3.42	64.6	56.4	58.1
	Y-Al-O	1.86 ($2\bar{2}01$)	1.86 ($0\bar{2}21$)	3.18 ($10\bar{1}0$)	57.7	61.2	61.2
Figure 5g	Measured	2.13	1.56	1.99	41.6	51.6	93.2
	Y ₂ Ti ₂ O ₇	1.87 ($\bar{4}40$)	1.68 (060)	1.87 (440)	45	45	90

During the SLM process, the local temperature increases above 2000 °C, which can melt the powders including Y_2O_3 . Moreover, the composition would be homogenized due to the Marangoni mixing effect in the melt pool. Thus, ideally, precipitation of Y-Ti-O particles occurs homogeneously within the melt pool. TEM analyses have been conducted on the SLM produced alloys to investigate the nano-particle characteristics. Figures 6a and b present the TEM micrographs of the SLM produced alloy. Similar to the compressed and sintered PM samples, there are nano-particles as well as larger irregular-shaped particles. However, as opposed to the PM samples, SLM results in micron-level grain size with micron/submicron level cellular structure (Figure 3g), rather than nano-grains. Figure 6c shows the HRTEM micrograph of a particle having a size of ~6-7 nm. Interplanar distances and angles have been determined from the HRTEM image in Figure 6d and FFT diffractogram in Figure 6e. The measured values match well with the interplanar spacing and angle of $Y_2Ti_2O_7$ particles, as seen in Table 4. Figures 6f and g show the HRTEM micrograph of a particle having a size of ~4 nm and the corresponding FFT diffractogram. Even though the lattice parameters are different than the parameters of $Y_2Ti_2O_7$ (PDF# 01-072-0302), the angles and ratio between the interplanar spacings are similar to pyrochlore structure; therefore, this particle is determined to be $Y_2Ti_2O_7$, as shown in Table 4. The reason for the smaller lattice parameter might be related to stoichiometry or composition. Similarly, Figure 6h shows the HRTEM micrograph of another small particle having a size of ~4 nm and the corresponding FFT diffractogram is presented in Figure 6i. This particle is also determined to be $Y_2Ti_2O_7$ even though the lattice parameter is smaller. Besides these fine oxides having sizes <5nm, there are coarser oxides that contain Al, as reported in Ref [33].

It has been observed that some particles are composed of multiple compositions or stoichiometry which results in crystallography change within the same particle in SLM produced alloy. For instance, in Figure 7a, the left and right parts of the particle have different crystallography. While the particle in Figure 7a has an incoherent interface around its periphery, the particle in Figure 7b exhibits a crystalline structure with semi-coherency with the matrix on the left side and a certain level of amorphization on the right side. A similar phenomenon which is called 'bi-phase' formation has been reported by Sinha et al in ODS IN617 alloys [43]. This has been attributed to the formation mechanisms of the Y-Al-O particles due to the reaction between Y_2O_3 and Al_2O_3 [44]. In other words, the existence of such particles infers incomplete transformation due to rapid cooling during SLM production.

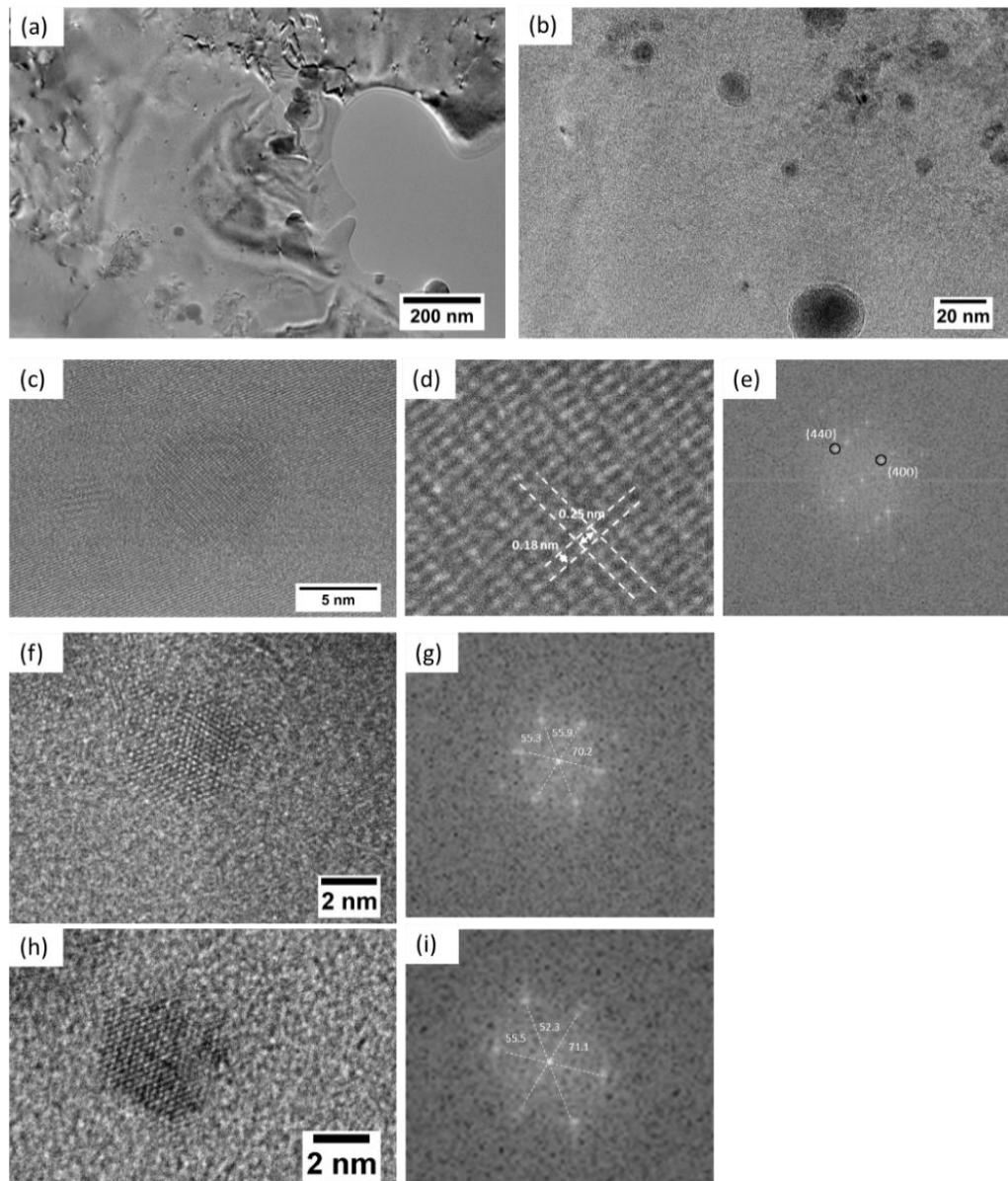


Figure 6. TEM micrographs of as-built SLM sample showing (a,b) the overall structure with nano-particles; HRTEM micrographs of (c,d) a particle with ~6-7 nm size and (e) corresponding FFT spectrum; (f,h) particles with ~4 nm size and (g,i) corresponding FFT spectra.

Table 4. Measured and theoretical interplanar distances and angles for the particles in Figure 6.

		d_1 (Å)	d_2 (Å)	d_3 (Å)	α_{12} (°)	α_{23} (°)	α_{13} (°)
Figure 6c	Measured	2.49	1.60	1.76	57.7	35.3	89.2
	$Y_2Ti_2O_7$	2.52 (400)	1.46 (44 $\bar{4}$)	1.78 (04 $\bar{4}$)	54.7	35.3	90
Figure 6f	Measured	2.53	2.2	2.55	55.3	55.9	70.2
	$Y_2Ti_2O_7$	2.9 ($\bar{2}\bar{2}\bar{2}$)	2.5 ($\bar{4}00$)	2.9 ($\bar{2}\bar{2}\bar{2}$)	54.7	54.7	70.5
Figure 6h	Measured	2.4	2.2	2.5	55.5	52.3	71.1
	$Y_2Ti_2O_7$	2.9 ($\bar{2}\bar{2}\bar{2}$)	2.5 ($\bar{4}00$)	2.9 ($\bar{2}\bar{2}\bar{2}$)	54.7	54.7	70.5

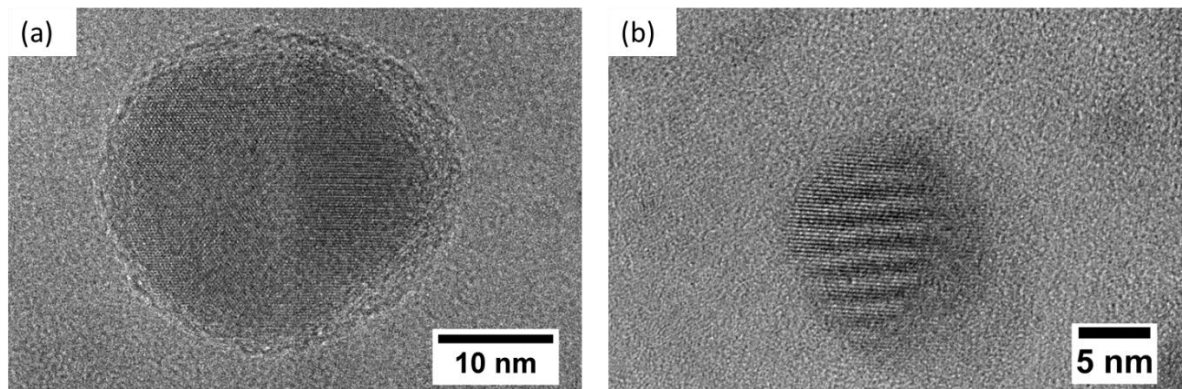


Figure 7. Two different particles having (a) crystallography district regions (b) coherency change within the same particle in SLM produced alloy.

The sizes of nano-particles (up to ~ 30 nm) were measured manually from the TEM images using the ImageJ v1.49 digital processing software including 75 to 150 counts for each foil. Number density which is defined as the number of particles per unit volume is calculated by assuming the foil thickness as 100 nm. When the nano-particles up to ~ 30 nm are considered, the particle size and number density graphs can be seen in Figure 8. The particle size of PM1250 sample is the smallest (~ 4 nm) while PM1500 and SLM samples have ~ 6 nm and ~ 5.2 nm, respectively. On the other hand, PM1500 has almost two times higher amount of nano-oxides with $\sim 3.5 \times 10^{22} \text{ m}^{-3}$, compared to PM1250. Moreover, the SLM sample has nano-particles having a number density of $\sim 2.5 \times 10^{22} \text{ m}^{-3}$. It should be noted that nano-particle distribution is relatively homogenous within the nano-grains in AM samples. On the other hand, the distribution of nano-particles is inhomogeneous in such a way that the particles precipitate in agglomerated clusters within the grain (or cell). Therefore, as the regions where the particles are populated are investigated, the number density is quite high compared to our previous study which considers the overall nano-particle distribution [33]. Moreover, high density-nanoparticles in the case of PM1500 sample result in higher hardness which is presented in Figure 2.

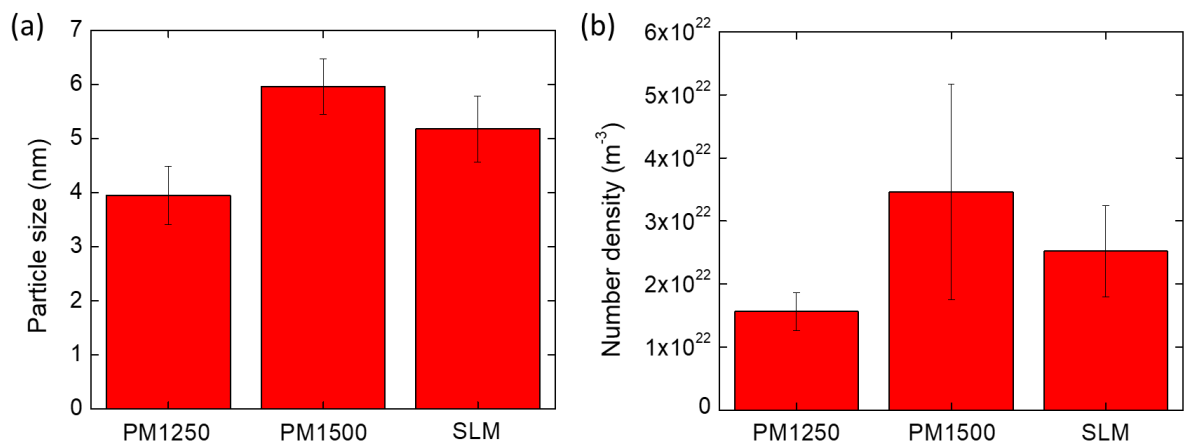


Figure 8. (a) Particle size and (b) number density of the nano-particles in PM and SLM samples.

4. CONCLUSIONS

In this study, oxide dispersion strengthened IN718 alloys have been produced using powder metallurgy and selective laser melting additive manufacturing. The effect of processing routes on the microstructure, in particular the nano-particle formation and structure has been investigated. It has been

found that compressing followed by sintering at 1250 and 1500 °C yields high density ODS alloys. The hardness of PM1500 sample is ~30 HV higher than that of PM1250 which is attributed to the lower nano-oxide number density in PM1250 alloy. It has been found that PM results in a nano-grained structure with nano-particles while SLM produced alloy has a larger cellular structure with Laves phase, carbides and oxides. The nano-particles have been determined to be $Y_2Ti_2O_7$, Y_2TiO_5 and/or $YTiO_3$ in PM1250 alloys while there are some Ni_2Y intermetallic particles as well as Y-Al-O and Y_2TiO_5 oxides. In the case of SLM produced alloy, fine $Y_2Ti_2O_7$ particles with smaller lattice parameter and larger size Y-Ti-Al-O particles have been observed. The PM1250, PM1500 and SLM samples have 4, 6 and 5.2 nm sized nano-oxides with $\sim 1.6 \times 10^{22} m^{-3}$, $\sim 3.5 \times 10^{22} m^{-3}$ and $\sim 2.5 \times 10^{22} m^{-3}$ number densities, respectively. It is noted that while the nano-oxides are distributed homogenously within nano-grains in PM samples, they exist in groups within the grain in the case of SLM sample. Besides, there are bi-phase particles in SLM produced alloys due to rapid cooling and incomplete transformation. This study shows that ODS IN718 alloys with high-density fine nano-oxides (<10 nm) can be produced using both powder metallurgy and additive manufacturing methods.

Declaration of Competing Interest

The authors declare that they have no known competing financial interests or personal relationships that could have appeared to influence the work reported in this paper.

Funding / Acknowledgements

This study is funded by LOREAL UNESCO For Women in Science 2021 Grant and the Scientific and Technological Research Council of Turkey (TUBITAK) under the grant No: 219M500.

REFERENCES

- [1] H. Zhang, C. Li, Q. Guo, Z. Ma, H. Li, and Y. Liu, "Improving creep resistance of nickel-based superalloy Inconel 718 by tailoring gamma double prime variants," *Scripta Materialia*, vol. 164, pp. 66-70, 2019/04/15/ 2019, doi: <https://doi.org/10.1016/j.scriptamat.2019.01.041>.
- [2] S. Pratheesh Kumar, S. Elangovan, R. Mohanraj, and J. R. Ramakrishna, "A review on properties of Inconel 625 and Inconel 718 fabricated using direct energy deposition," *Materials Today: Proceedings*, vol. 46, pp. 7892-7906, 2021/01/01/ 2021, doi: <https://doi.org/10.1016/j.matpr.2021.02.566>.
- [3] E. Aydogan *et al.*, "Effect of tube processing methods on microstructure, mechanical properties and irradiation response of 14YWT nanostructured ferritic alloys," *Acta Materialia*, vol. 134, pp. 116-127, 2017/08/01/ 2017, doi: <https://doi.org/10.1016/j.actamat.2017.05.053>.
- [4] E. Aydogan, O. El-Atwani, S. Takajo, S. C. Vogel, and S. A. Maloy, "High temperature microstructural stability and recrystallization mechanisms in 14YWT alloys," *Acta Materialia*, vol. 148, pp. 467-481, 2018/04/15/ 2018, doi: <https://doi.org/10.1016/j.actamat.2018.02.006>.
- [5] G. R. Odette, "Recent Progress in Developing and Qualifying Nanostructured Ferritic Alloys for Advanced Fission and Fusion Applications," *JOM*, Article in Press 2014, doi: 10.1007/s11837-014-1207-5.
- [6] G. R. Odette, M. J. Alinger, and B. D. Wirth, "Recent Developments in Irradiation-Resistant Steels," *Annual Review of Materials Research*, vol. 38, no. 1, pp. 471-503, 2008, doi: 10.1146/annurev.matsci.38.060407.130315.
- [7] T. Chen *et al.*, "Microstructural changes and void swelling of a 12Cr ODS ferritic-martensitic alloy after high-dpa self-ion irradiation," *Journal of Nuclear Materials*, Article vol. 467, pp. 42-49, 2015, Art no. 49325, doi: 10.1016/j.jnucmat.2015.09.016.

- [8] Y. Wu, E. M. Haney, N. J. Cunningham, and G. R. Odette, "Transmission electron microscopy characterization of the nanostructures in nanostructured ferritic alloy MA957," *Acta Materialia*, vol. 60, no. 8, pp. 3456-3468, 5// 2012, doi: <http://dx.doi.org/10.1016/j.actamat.2012.03.012>.
- [9] Z. Zhang, T. A. Saleh, S. A. Maloy, and O. Anderoglu, "Microstructure evolution in MA956 neutron irradiated in ATR at 328 °C to 4.36 dpa," *Journal of Nuclear Materials*, vol. 533, p. 152094, 2020/05/01/ 2020, doi: <https://doi.org/10.1016/j.jnucmat.2020.152094>.
- [10] C. W. Park, J. M. Byun, W. J. Choi, S. Y. Lee, and Y. D. Kim, "Improvement of high temperature mechanical properties of Ni-based oxide dispersion strengthened alloys by preferential formation of Y-Ti-O complex oxide," *Materials Science and Engineering: A*, vol. 740-741, pp. 363-367, 2019/01/07/ 2019, doi: <https://doi.org/10.1016/j.msea.2018.10.004>.
- [11] N. J. Cunningham *et al.*, "Effect of bulk oxygen on 14YWT nanostructured ferritic alloys," *Journal of Nuclear Materials*, vol. 444, no. 1, pp. 35-38, 2014/01/01/ 2014, doi: <https://doi.org/10.1016/j.jnucmat.2013.09.013>.
- [12] D. T. Hoelzer, J. Bentley, M. A. Sokolov, M. K. Miller, G. R. Odette, and M. J. Alinger, "Influence of particle dispersions on the high-temperature strength of ferritic alloys," *Journal of Nuclear Materials*, vol. 367-370, pp. 166-172, 2007/08/01/ 2007, doi: <https://doi.org/10.1016/j.jnucmat.2007.03.151>.
- [13] S. Ukai and M. Fujiwara, "Perspective of ODS alloys application in nuclear environments," *Journal of Nuclear Materials*, vol. 307-311, pp. 749-757, 2002/12/01/ 2002, doi: [https://doi.org/10.1016/S0022-3115\(02\)01043-7](https://doi.org/10.1016/S0022-3115(02)01043-7).
- [14] M. K. Miller, D. T. Hoelzer, E. A. Kenik, and K. F. Russell, "Stability of ferritic MA/ODS alloys at high temperatures," *Intermetallics*, vol. 13, no. 3, pp. 387-392, 2005/03/01/ 2005, doi: <https://doi.org/10.1016/j.intermet.2004.07.036>.
- [15] L. Yu *et al.*, "Effects of Al content on microstructure and tensile properties of Ni-based ODS superalloys," *Journal of Alloys and Compounds*, vol. 941, p. 168965, 2023/04/25/ 2023, doi: <https://doi.org/10.1016/j.jallcom.2023.168965>.
- [16] E. Hosseini and V. A. Popovich, "A review of mechanical properties of additively manufactured Inconel 718," *Additive Manufacturing*, vol. 30, p. 100877, 2019/12/01/ 2019, doi: <https://doi.org/10.1016/j.addma.2019.100877>.
- [17] M. M. Attallah, R. Jennings, X. Wang, and L. N. Carter, "Additive manufacturing of Ni-based superalloys: The outstanding issues," *MRS Bulletin*, vol. 41, no. 10, pp. 758-764, 2016/10/01 2016, doi: 10.1557/mrs.2016.211.
- [18] M. Ni *et al.*, "Microstructure and mechanical properties of additive manufactured Inconel 718 alloy strengthened by oxide dispersion with 0.3 wt% Sc addition," *Journal of Alloys and Compounds*, vol. 918, p. 165763, 2022/10/15/ 2022, doi: <https://doi.org/10.1016/j.jallcom.2022.165763>.
- [19] J. P. Oliveira, A. D. LaLonde, and J. Ma, "Processing parameters in laser powder bed fusion metal additive manufacturing," *Materials & Design*, vol. 193, p. 108762, 2020/08/01/ 2020, doi: <https://doi.org/10.1016/j.matdes.2020.108762>.
- [20] M. Ni, S. Liu, C. Chen, R. Li, X. Zhang, and K. Zhou, "Effect of heat treatment on the microstructural evolution of a precipitation-hardened superalloy produced by selective laser melting," *Materials Science and Engineering: A*, vol. 748, pp. 275-285, 2019/03/04/ 2019, doi: <https://doi.org/10.1016/j.msea.2019.01.109>.
- [21] V. A. Popovich, E. V. Borisov, A. A. Popovich, V. S. Sufiiarov, D. V. Masaylo, and L. Alzina, "Impact of heat treatment on mechanical behaviour of Inconel 718 processed with tailored microstructure by selective laser melting," *Materials & Design*, vol. 131, pp. 12-22, 2017/10/05/ 2017, doi: <https://doi.org/10.1016/j.matdes.2017.05.065>.
- [22] W. Tillmann, C. Schaak, J. Nellesen, M. Schaper, M. E. Aydinöz, and K. P. Hoyer, "Hot isostatic pressing of IN718 components manufactured by selective laser melting," *Additive Manufacturing*, vol. 13, pp. 93-102, 2017/01/01/ 2017, doi: <https://doi.org/10.1016/j.addma.2016.11.006>.

- [23] J. Deng, C. Chen, X. Liu, Y. Li, K. Zhou, and S. Guo, "A high-strength heat-resistant Al-5.7Ni eutectic alloy with spherical Al₃Ni nano-particles by selective laser melting," *Scripta Materialia*, vol. 203, p. 114034, 2021/10/01/ 2021, doi: <https://doi.org/10.1016/j.scriptamat.2021.114034>.
- [24] D.-R. Liu, S. Wang, and W. Yan, "Grain structure evolution in transition-mode melting in direct energy deposition," *Materials & Design*, vol. 194, p. 108919, 2020/09/01/ 2020, doi: <https://doi.org/10.1016/j.matdes.2020.108919>.
- [25] S. Xu *et al.*, "Combination of back stress strengthening and Orowan strengthening in bimodal structured Fe-9Cr-Al ODS steel with high Al addition," *Materials Science and Engineering: A*, vol. 739, pp. 45-52, 2019/01/02/ 2019, doi: <https://doi.org/10.1016/j.msea.2018.09.111>.
- [26] S. Ukai *et al.*, "Directional recrystallization by zone annealing in a Ni-based ODS superalloy," *Journal of Alloys and Compounds*, vol. 744, pp. 204-210, 2018/05/05/ 2018, doi: <https://doi.org/10.1016/j.jallcom.2018.01.406>.
- [27] A. Ozsoy, E. Aydogan, and A. F. Dericioglu, "Selective laser melting of Nano-TiN reinforced 17-4 PH stainless steel: Densification, microstructure and mechanical properties," *Materials Science and Engineering: A*, vol. 836, p. 142574, 2022/03/02/ 2022, doi: <https://doi.org/10.1016/j.msea.2021.142574>.
- [28] E. Vasquez *et al.*, "Elaboration of oxide dispersion strengthened Fe-14Cr stainless steel by selective laser melting," *Journal of Materials Processing Technology*, vol. 267, pp. 403-413, 2019/05/01/ 2019, doi: <https://doi.org/10.1016/j.jmatprotec.2018.12.034>.
- [29] C. Guo, Z. Yu, C. Liu, X. Li, Q. Zhu, and R. Mark Ward, "Effects of Y₂O₃ nanoparticles on the high-temperature oxidation behavior of IN738LC manufactured by laser powder bed fusion," *Corrosion Science*, vol. 171, p. 108715, 2020/07/15/ 2020, doi: <https://doi.org/10.1016/j.corsci.2020.108715>.
- [30] R. Xu *et al.*, "Microstructure and mechanical properties of in-situ oxide-dispersion-strengthened NiCrFeY alloy produced by laser powder bed fusion," *Advanced Powder Materials*, vol. 1, no. 4, p. 100056, 2022/10/01/ 2022, doi: <https://doi.org/10.1016/j.apmate.2022.100056>.
- [31] J. U. Rakhmonov, C. Kenel, A. De Luca, C. Leinenbach, and D. C. Dunand, "Effect of Y₂O₃ dispersoids on microstructure and creep properties of Hastelloy X processed by laser powder-bed fusion," *Additive Manufacturing Letters*, vol. 3, p. 100069, 2022/12/01/ 2022, doi: <https://doi.org/10.1016/j.addlet.2022.100069>.
- [32] E. Aydogan *et al.*, "In-situ radiation response of additively manufactured modified Inconel 718 alloys," *Additive Manufacturing*, vol. 51, p. 102601, 2022/03/01/ 2022, doi: <https://doi.org/10.1016/j.addma.2022.102601>.
- [33] M. Yesim Yalcin, D. Bora, and E. Aydogan, "Development and additive manufacturing of oxide dispersion strengthened inconel 718: Thermochemical and experimental studies," *Journal of Alloys and Compounds*, vol. 914, p. 165193, 2022/09/05/ 2022, doi: <https://doi.org/10.1016/j.jallcom.2022.165193>.
- [34] B. Y. v. B. E. U. Karakılınç "Toz Yataklı/Beslemeli Eklemeli İmalatta Kullanılan Partiküllerin Uygunluk Araştırması ve Partikül İmalat Yöntemleri," *Politeknik Dergisi*, vol. 22, no. 4, pp. 801-810, 2019, doi: 10.2339/politeknik.423707.
- [35] T. Chen *et al.*, "Temperature dependent dispersoid stability in ion-irradiated ferritic-martensitic dual-phase oxide-dispersion-strengthened alloy: Coherent interfaces vs. incoherent interfaces," *Acta Materialia*, vol. 116, pp. 29-42, 2016/09/01/ 2016, doi: <https://doi.org/10.1016/j.actamat.2016.05.042>.
- [36] Y. Miao *et al.*, "The interfacial orientation relationship of oxide nanoparticles in a hafnium-containing oxide dispersion-strengthened austenitic stainless steel," *Materials Characterization*, vol. 101, pp. 136-143, 2015/03/01/ 2015, doi: <https://doi.org/10.1016/j.matchar.2015.01.015>.
- [37] M. Mujahid and J. W. Martin, "The effect of oxide particle coherency on Zener pinning in ODS superalloys," *Journal of Materials Science Letters*, vol. 13, no. 3, pp. 153-155, 1994/01/01 1994, doi: 10.1007/BF00278146.

- [38] L. F. He *et al.*, "Mechanical properties of Y₂Ti₂O₇," *Scripta Materialia*, vol. 64, no. 6, pp. 548-551, 2011/03/01/ 2011, doi: <https://doi.org/10.1016/j.scriptamat.2010.11.042>.
- [39] K. Mo *et al.*, "Synchrotron study on load partitioning between ferrite/martensite and nanoparticles of a 9Cr ODS steel," *Journal of Nuclear Materials*, vol. 455, no. 1, pp. 376-381, 2014/12/01/ 2014, doi: <https://doi.org/10.1016/j.jnucmat.2014.06.060>.
- [40] G. Moskal *et al.*, "Microstructural characterization of laser-cladded NiCrAlY coatings on Inconel 625 Ni-based superalloy and 316L stainless steel," *Surface and Coatings Technology*, vol. 387, p. 125317, 2020/04/15/ 2020, doi: <https://doi.org/10.1016/j.surfcoat.2019.125317>.
- [41] N. Mattern, M. Zinkevich, W. Löser, G. Behr, and J. Acker, "Experimental and thermodynamic assessment of the Nb-Ni-Y system," *Journal of Phase Equilibria and Diffusion*, Article vol. 29, no. 2, pp. 141-155, 2008, doi: 10.1007/s11669-007-9243-2.
- [42] Y. Zhou, M. Hu, P. Yan, X. Shi, X. Chong, and J. Feng, "A first-principles calculation of structural, mechanical, thermodynamic and electronic properties of binary Ni-Y compounds," *RSC Advances*, Article vol. 8, no. 72, pp. 41575-41586, 2018, doi: 10.1039/c8ra09383k.
- [43] S. K. Sinha, A. Dasgupta, M. Sivakumar, C. Ghosh, and S. Raju, "Unraveling the Complexity of Nano-Dispersoids in the Oxide Dispersion Strengthened Alloy 617," *Microscopy and Microanalysis*, vol. 28, no. 5, pp. 1463-1471, 2022, doi: 10.1017/S143192762200071X.
- [44] M. Sivakumar, S. K. Sinha, A. Dasgupta, and S. M. Shaikh, "Structure and Texture of Oxide Dispersion Strengthened Alloy 617 for Very High Temperature Applications," *Metallurgical and Materials Transactions A*, vol. 52, no. 11, pp. 4974-4986, 2021/11/01 2021, doi: 10.1007/s11661-021-06442.